PAPER

Check for updates

Alkali metal borate conjugated block polyelectrolytes as tuneable mixed ionic-electronic conductors

Sebastian J. Leeming, Samuel Fryer [ID] † and Georgina L. Gregory [ID] *

Conjugated polyelectrolytes (CPEs) combine ionic conductivity from tethered ionic groups with electronic conductivity from intrinsically-doped π-conjugated backbones, enabling applications in energy storage, bioelectronics, and neuromorphic computing. Conjugated block polyelectrolytes (CBEs), in which the conjugated and ionic functions are spatially segregated into distinct blocks, represent an emerging and underexplored variant of this materials class. Despite multiple studies of various pendant ionic groups, neither borate ionic functionalisation nor block copolymer architectures bearing non-sulfonate ionic groups have been explored. Here, we report CBEs, accessible through controlled Suzuki−Miyaura catalyst-transfer polymerisation (SCTP) and cyclic carbonate ring-opening polymerisation (ROP), incorporating alkali metal borate polycarbonate segments: poly(3-hexylthiophene)-*block*-poly(ethylene oxide-*graft*-poly(ethylene glycol))-*block*-polycarbonate bearing lithium, sodium, or potassium borate moieties. Systematic variation of P3HT chain length (DP = 35 and 110) and content (10−50 wt%) reveals distinct cation-dependent transport behaviour. Electrochemical characterisation *via* impedance spectroscopy, chronoamperometry, and linear sweep voltammetry demonstrates purely ionic conduction at low applied potentials, with p-type electronic transport activated above 1−1.5 V. Notably, lithium-ion conductivity remains independent of P3HT incorporation, whereas sodium transport improves with longer conjugated blocks and potassium conductivity is enhanced with shorter segments. Thermal analysis, DFT calculations, rheological and tensile measurements establish structure−property relationships linking polymer ionic networking to mechanical and ionic-electronic transport properties. These findings position anionic borate CBEs as a promising addition to the mixed ionic-electronic conductor platform, with tuneable properties for emerging electrochemical technologies and a modular synthetic approach expected to extend to alternative conjugated backbones and other polyelectrolyte groups easily installed by ligand coordination chemistry.

Introduction

Polymers capable of conducting both ions and electrons have emerged as promising materials underpinning a variety of societally impactful technologies, including energy-saving smart windows,[1] next-generation energy storage,[2] bioelectronics,[3,4] solar cells,[5] and brain-mimicking neuromorphic devices.[6] In rechargeable batteries, this dual conductivity has been exploited in polymeric electrode binders to promote ion transport through to the electrolyte and electronic conductivity to the external circuit, with potential extension to wearable devices.[7–9] At bioelectronic interfaces, such materials lie at the heart of communication between biological systems that employ ions (Na+, K+) and external electronic readouts.[10,11] In organic electrochemical transistors, which exploit ion flux to modulate electronic transport, mixed conductors have enabled biosensor development[12] and even shown diagnostic promise for neurodegenerative diseases.[13] While blends such as the archetypal mixed conductor poly(3,4-ethylenedioxythiophene):poly(styrene sulfonate) (PEDOT:PSS) have proven highly effective in such applications, conjugated polyelectrolytes (CPEs), which incorporate ionic pendant groups directly onto electrically conducting conjugated backbones, are increasingly attractive as single-component, synthetically tailorable ionic-electronic conductors.[10,14–16] Their unified architecture provides multiple design handles, including backbone structure,[5,17] side-chain chemistry,[18–20] ionic group identity[21] and density,[22] plus counterion selection.[23–25] The ionic functionality confers solubility in polar solvents (enabling, for example, water-soluble CPEs for antibacterial applications[26]) and facilitates self-doping, enhancing conduc-

Chemistry Research Lab, University of Oxford, 12 Mansfield Road, Oxford, OX1 3TA, UK. E-mail: georgina.gregory@chem.ox.ac.uk
†Current address: School of Chemistry, University of Bristol, Bristol, BS8 1TS, UK.

tivity without exogenous additives. Nevertheless, the library of CPE structures remains relatively narrow, and more systematic studies correlating molecular design with ionic and electronic transport are required.[27]

CPE properties arise from an interplay of ionic and electronic transport behaviours that depend on distinct yet coupled design features.[28] Electrical conductivity along conjugated polymer backbones relies on delocalised π-systems, though the intrinsic conductivity of undoped conjugated polymers is low. In p-type doping (oxidation), removal of an electron from the π-system creates a radical cation; this species, together with associated bond structure distortions, is termed a polaron.[29] In anionic CPEs, pendant anionic groups stabilise these positive polarons through electrostatic interactions, enabling self-doping and thus enhancing electrical conductivity, a well-established characteristic of such materials.[14,30–32] The mobile countercations, meanwhile, provide ionic conductivity, rendering anionic CPEs single-ion conductors in which the fixed anionic group is immobile while the counterion carries charge. Ion transport is generally favoured by flexible backbones with low glass transition temperatures that facilitate segmental dynamics, with factors such as ion dissociation playing a critical role;[33] single-ion conducting trifluoromethanesulfonimide-based polyanions exemplify this principle.[34] A well-studied example is CPE-K (poly[2,6-(4,4-bis-potassium butanylsulfonate-4H-cyclopenta-[2,1-b;3,4-b′]-dithiophene)-alt-4,7-(2,1,3-benzothiadiazole)]), in which sulfonate anions stabilise polarons on the dithiophene-benzothiadiazole conjugated backbone while K$^+$ countercations provide ionic transport.[6,30,31,35] Investigations of CPE-K variants with different cations (Li$^+$, Na$^+$, K$^+$, Cs$^+$, Al^{3+}) reveal that cation–anion pairing affects both conductivity and self-doping efficiency, with Na$^+$ yielding optimal performance.[23,32] While various cationic CPEs have been investigated,[21] most recently phosphonium-substituted CPEs exhibiting antibacterial properties,[26] carboxylates and sulfonates have dominated the palette of anionic groups examined, including polythiophenes bearing variously functionalised side chains (alkyl, oligoethylene oxide, ester, hydroxy, and carboxylic acid) with different potassium salts.[36] In contrast, in pure polyelectrolytes, borates have emerged as attractive pendant anions for ionic conductivity owing to better charge delocalisation and weaker cation pairing characteristics[37–40] that may also leave the anion more available for polaron stabilisation. Indeed, in semiconducting polymers doped with BF$_4^-$ and BArF$^-$ salts, larger anions have been shown to enhance properties in regioregular P3HT by reducing coulombic interactions.[41] The identity of the pendant anionic functionality is therefore important both for stabilising polarons in p-type conductors and for promoting counterion dissociation to enable ionic mobility.

Beyond ionic group identity, side chains also influence molecular packing, which is critical for electronic transport; charge transfer occurs not only along conjugated backbones but also via intermolecular hopping between adjacent chains, and packing disruptions can impede this process.[42] Poly(3-hexylthiophene) (P3HT) serves as a model conjugated polymer

owing to its solution processability, scalable synthesis, and well-characterised structure–property relationships. Graft copolymers such as P3HT-g-poly(acrylic acid) (P3HT-g-PAA)[43] and P3HT-g-poly(ethylene oxide) (P3HT-g-PEO)[44] demonstrate that pendant chains can disrupt structural order and backbone mobility, potentially compromising π–π stacking and electronic transport.[45] The precise connectivity of ion-coordinating side chains to the backbone also influences ion transport, as demonstrated in polythiophenes bearing oligoethylene glycol substituents.[46] Block copolymers offer an alternative architecture that may introduce ionic functionality while minimising disruption to conjugated block packing.[8] P3HT-b-PEO has been investigated because the PEO segment aids processing and, when combined with lithium salts, imparts ionic conductivity.[47,48] Notably, in poly(3-hexylthiophene)-block-poly(oligo-oxyethylene methacrylate) (P3HT-b-POEM), interactions with ionic species significantly improve molecular order and unexpectedly induce oxidative doping of the P3HT block in both solution and solid states.[49] The choice of the non-conjugated block also matters: P3HT-b-poly(n-butyl acrylate) (P3HT-b-PBA) experiences minimal structural disorder upon electrolyte swelling, maintaining its original structure better than either P3HT homopolymer or the more hydrophilic P3HT-b-PEO, with the hydrophobic nature of PBA contributing to backbone stability.[50] However, these examples rely on added salts or external ionic species rather than incorporating ionic functionality directly into the polymer structure. True conjugated block polyelectrolytes (CBEs), combining a conjugated block with a neighbouring covalently tethered ionic block, could unite the architectural advantages of block copolymers with the self-doping and single-ion conduction of CPEs. P3HT-based block polyelectrolytes bearing styrenesulfonate groups (P3HT-b-PSS) have been reported via routes including click chemistry of separate polymers[51,52] and controlled radical polymerisation,[53] with improved conductivities attributed in part to self-doping by the PSS block.[54] However, borate-functionalised CBEs, which offer potential advantages in charge delocalisation and cation dissociation relative to sulfonate analogues, have not yet been explored.

Suzuki–Miyaura catalyst-transfer polymerisation (SCTP), pioneered by the Lee and Choi groups, is an attractive strategy for accessing well-defined P3HT-based block copolymers.[55–57] SCTP delivers a living-type polymerisation, producing P3HT of controlled molar mass and high regioregularity with critically high end-group fidelity. The method employs a Pd precatalyst and an N-methyliminodiacetic acid (MIDA) boronate-protected 3-hexylthiophene monomer, operating under mild conditions to grow P3HT from aryl-iodide initiators.[55,57] The chemistry extends beyond thiophene to various donor/acceptor heteroarenes.[58] Rod-coil block copolymers have been accessed by initiating SCTP from iodide-terminated coil polymers,[59] and coupling SCTP with another living polymerisation, atom transfer radical polymerisation (ATRP) via a bifunctional initiator allows further architectural control.[60] Notably, bifunctional iodobenzyl alcohol initiators permit protection-free synthesis of hydroxyl-terminated P3HT.[61] The high hydroxyl end-group

fidelity presents an opportunity for subsequent chain extension by the controlled catalysed ring-opening polymerisation (ROP) of cyclic monomers. Separately, alcohol-initiated ROP of a vinyl-functional cyclic carbonate has been used to produce polycarbonates that, as we previously reported, can subsequently be converted into lithium borate polyelectrolytes.[39] These borate polycarbonate polyelectrolytes are synthetically accessible non-fluorinated single-ion conductors, that benefit from large, charge-delocalised borate anions. Combining this borate chemistry with SCTP-derived P3HT blocks therefore presents an attractive route to borate-functionalised CBEs.

Herein, we report the synthesis of anionic borate CBEs comprising P3HT and polyelectrolytes with lithium, sodium, and potassium countercations. Using SCTP, P3HT-OH macroinitiators of various degrees of polymerisation (DP), particularly DP = 35 and 110, are employed for one-pot sequential ROP of a polyethylene glycol (PEG)-derivatised epoxide (PEG average M_n of 2 kg mol^{-1}) and a vinyl-functional cyclic carbonate. This yields pseudo-ABC triblock copolymers where A = P3HT, B = P(EO-g-PEG), and C = lithium, sodium, or potassium borate polycarbonate after modification of the pendant vinyl groups through thiol–ene and boron coordination chemistry. Incorporation of a PEO-g-PEG intermediate block aids ionic conductivity through coordination to the alkali metal cations and improves solubility of the P3HT macroinitiator, motivating the triblock over diblock design. The thermal properties of the polymer films are characterised by differential scanning calorimetry (DSC) and thermogravimetric analysis (TGA), revealing trends in glass transition temperature (T_g) with alkali metal cation identity; the cation also influences interchain cross-linking to form networks, the mechanical properties of which are evaluated by rheology and uniaxial tensile testing. The efficiency of these polymers as solid-state ionic conductors, facilitated by the B-block ether coordinating environment and supported by DFT calculations, and the influence of the conjugated block on ion transport for the different cations are assessed by electrochemical impedance spectroscopy (EIS), with further insights provided by dielectric relaxation spectroscopy (DRS). Electrical properties are probed by linear sweep voltammetry (LSV) and chronoamperometry (CA), revealing that onset voltage for electronic conduction is tuneable through cation selection and P3HT DP. Finally, the synthetic methodology is extended to block copolymers spanning 10, 20, and 50 wt% P3HT.

Experimental

General procedure for P3HT-b-P(EO-g-PEG)-b-PAEC

P3HT-OH macroinitiators were synthesised from M1 via SCTP following the literature procedures for M1[62] and SCTP (see SI for experimental details and Table S1 for precise monomer-to-initiator ratios).[59] AEC was synthesised as described elsewhere.[63] To the P3HT-OH macroinitiator (DP = 35; 153.9 mg, 0.028 mmol, 1 equiv.) dissolved in THF (5 mL) was added the methoxypolyethylene glycol epoxide (PEG average M_n 2 kg

mol^{-1}, mPEG-EPO; 0.276 g, 0.138 mmol, 5 equiv.) and AEC (2.76 g, 13.8 mmol, 500 equiv.) monomers, followed by tBu-P4 catalyst (138 μL, 0.8 M in hexanes, 0.028 mmol, 1 equiv.). The solution was then added to a preheated oil bath at 60 °C and stirred for ca. 4 h until full conversion of the epoxide monomer as determined by ^{1}H NMR spectroscopy (CDCl$_3$) of aliquots (loss of signals at δ = 2.60, 2.78 and 3.15 ppm). The still-stirring reaction mixture was then cooled to room temperature and concentrated until 80–90% cyclic carbonate conversion. The catalyst was then quenched by addition of acetic acid (ca. 10 equiv. relative to catalyst) and the reaction mixture precipitated into cold pentane and washed with petroleum ether (×3) to yield a red/purple paste (ca. 3.2 g).

General procedure for Li-, Na- and K-borate CBEs

Under inert atmosphere, to the vinyl triblock polymer (e.g., for PT35 series: 3.2 g, 9.6 mmol C=C, 1 equiv. C=C), dissolved in degassed MeCN (15 mL, 0.2 g mL^{-1}), was added mercaptosuccinic acid (MSA; 2.88 g, 19.2 mmol, 2 equiv.) and 2,2-dimethoxy-2-phenylacetophenone (DMPA; 0.492 g, 1.92 mmol, 0.2 equiv.). The solution was stirred for 2 h under UV light (λ = 365 nm), during which time the now diacid functionalised polymer precipitated out of solution. Decantation of the MeCN and multiple washings of the resulting residue with diethyl ether and MeCN followed by drying in vacuo afforded an adhesive purple material (quantitative yield) that was used in the subsequent step without further purification.

Under an argon atmosphere, the now diacid-functionalised polymer (e.g., for PT35: ca. 5.29 g) was dissolved in anhydrous DMSO (90 mL). The solution was divided into three equal portions by volume (e.g., for PT35: 30 mL, 1.76 g, 5.04 mmol MSA, 1 equiv. MSA). To each portion, B(OH)$_3$ (234 mg, 3.78 mmol, 1.5 equiv.) and M$_2$CO$_3$ (1.89 mmol, 0.75 equiv., where M = Li, Na, or K at 140, 201 or 270 mg, respectively) was added. The solution was stirred at 60 °C for 12 h, cooled to RT, and the polymer isolated by precipitation into diethyl ether. The borate polymers were further purified by washing with diethyl ether and MeCN (×3) before being dried under vacuum (10^{-3} mbar) for 24–48 h, until constant mass.

Results and discussion

Conjugated polyelectrolyte synthesis and characterisation

To access CBEs based on P3HT and alkali metal borate polyelectrolytes (CBE-BO$_4^-$M$^+$ where M = Li$^+$, Na$^+$ and K$^+$), P3HT-OH macroinitiators were first synthesised via SCTP using M1 monomer (5-bromo-4-n-hexylthien-2-yl-MIDA-boronate) and a 4-iodobenzyl alcohol bifunctional initiator (Fig. 1A). M1 is a bench-stable MIDA-protected boronate ester that undergoes slow hydrolysis during polymerisation to release the active boronic acid species.[44] Chain growth is initiated by a RuPhos-Pd G3 catalyst in the presence of K$_3$PO$_4$ (see SI for proposed mechanism).[45,46] Crucially, SCTP proceeds unidirectionally from the iodo-terminus of the initiator, leaving the benzyl alcohol functionality intact for subsequent
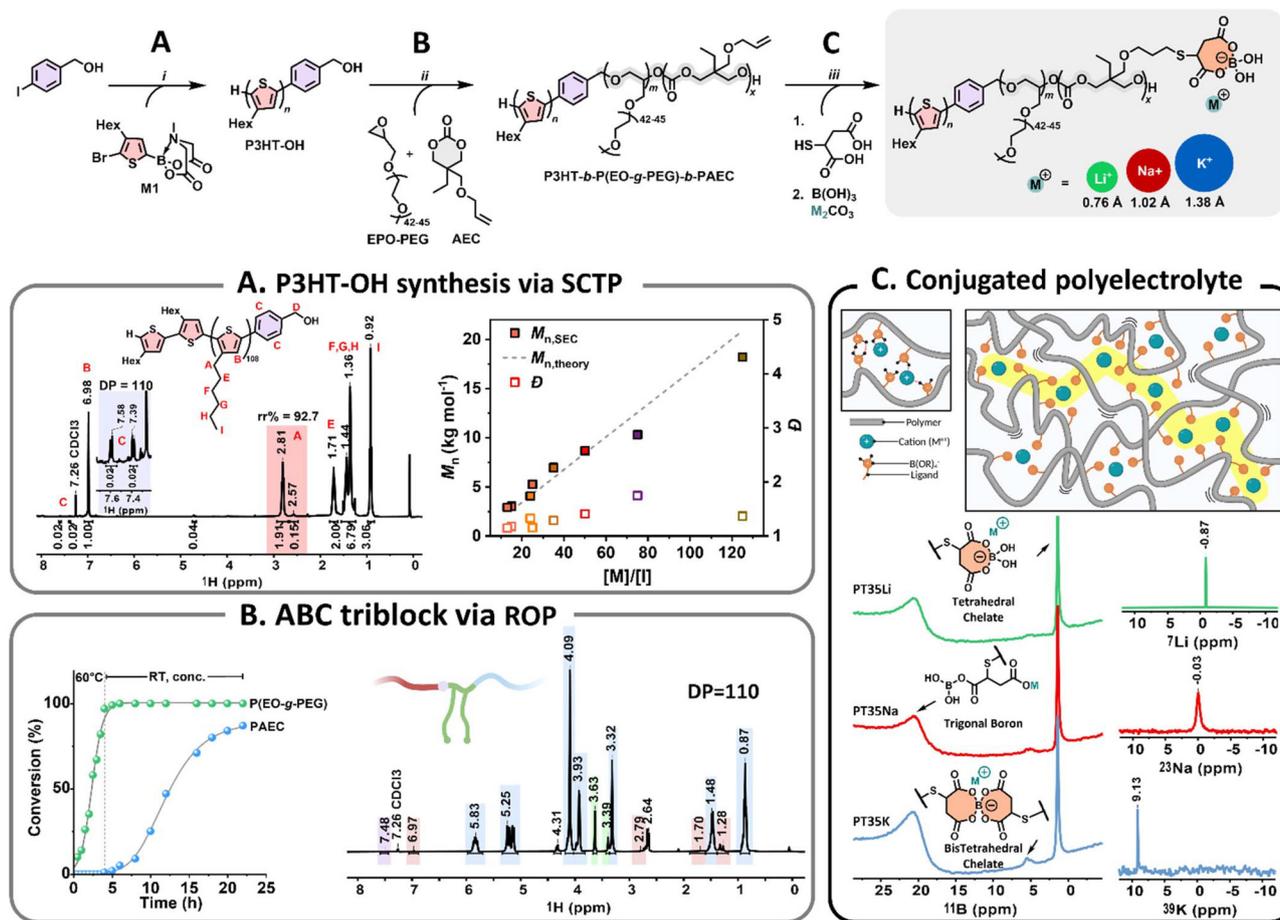
Fig. 1 Synthetic scheme for (A) SCTP synthesis of P3HT-OH macroinitiators for (B) chain growth to form ABC-triblock polymers in one-pot, which are converted to (C) polyelectrolytes *via* thiol−ene chemistry and alkali metal borate formation. For (A), ^{1}H NMR spectra (CDCl₃) highlights regioregularity (rr) and DP determination for P3HT-OH (DP = 110) with control over M_n achieved by the M1-to-iodobenzyl alcohol initiator ratio. For (B), conversion time showing ROP of EPO-PEG to P(EPO-*g*-PEG) (green) at elevated temperatures followed by AEC ROP to PAEC (blue) under cooled and concentrated reaction conditions to yield isolated products with representative ^{1}H NMR (CDCl₃) shown. For CBEs (C), ^{11}B{^{1}H} NMR spectra (DMSO-d₆) showing borate environments alongside ^{7}Li, ^{23}Na or [39]K NMR spectra for PT35Li, PT35Na and PT35K (P3HT DP = 35), respectively confirming single cation environments.

macroinitiation. The mechanism also ensures preferential head-to-tail (HT) couplings, affording regioregular (rr) P3HT which is important for optimising electrical properties as it affords extended planar conjugated backbones associated with high charge carrier mobilities.[8]

The degree of polymerisation (DP) was readily controlled by varying the monomer-to-initiator ([M]/[I]) ratio, with a characteristic colour progression from orange to purple in CHCl₃ solution with increasing DP; the highest DP samples (DP = 110) formed gold-coloured free-standing films. End-group fidelity and controlled chain growth were verified by multiple complementary techniques. First, M_n values determined by ^{1}H NMR spectroscopy, through integration of the benzyl aromatic resonances (7.59 and 7.39 ppm) against the thiophene ring environment at 6.98 ppm, showed good agreement with both theoretical values based on [M]/[I] and with those measured by size exclusion chromatography ($M_{n,SEC}$) across multiple ratios tested. Regioregularity was quantified by ^{1}H NMR analysis of

the α-methylene region (2.81–2.57 ppm), revealing >86% HT content. MALDI-ToF mass spectrometry further confirmed the presence of the expected benzyl alcohol end-group, with the major series corresponding to P3HT chains bearing the 4-hydroxymethylphenyl initiator fragment and H termini (Fig. S2). Two P3HT chain lengths were selected for this study, DP = 35 and DP = 110, corresponding to $M_{n,NMR}$ values of 5.6 and 18.0 kg mol⁻¹ respectively with regioregularities of 90 and 93% ($M_{n,SEC}$ = 7.0 and 18.2 kg mol⁻¹; $M_{n,theory}$ = 6.0 and 18.5 kg mol⁻¹; Table 1).

These P3HT-OH macroinitiators were chain-extended by one-pot sequential ROP of two cyclic monomers: PEG-functionalised epoxide (EPO-PEG, 44–45 EO units long) and 2-allyloxymethyl-2-ethyltrimethylene carbonate (AEC) (Fig. 1B), using *t*Bu-P4 phosphazene base as organocatalyst (see SI for ROP mechanism). Since cyclic carbonate ROP is governed by equilibrium thermodynamics, whereby polymer formation is favoured at high monomer concentrations and lower

Table 1 Anionic borate CBEs: varying P3HT DP

CBE-BO$_4^-$M$^+$	$M_{n,NMR}$ (kg mol^{-1}) P3HT-OH[a]	Electronic block[b] (wt%)	Ionic blocks[b] (wt%)	$M_{n,SEC}$[c] (kg mol^{-1})	$Đ$[c]
PT0	0.0	0	100	111.2	1.59
PT35	5.6	9	91	96.3	1.88
PT110	18.0	12	88	108.6	2.01

[a] Determined by relative integration of benzyl initiator to 3HT ^{1}H NMR environments (Fig. 1a & S1). [b] Composition based on relative ^{1}H NMR integration and repeat unit masses of 166 g mol^{-1} for electronic P3HT, and ionic: P(EO-g-PEG) (ca. 2000 g mol^{-1}) plus PAEC (200 g mol^{-1}). [c] Measured by SEC (RI detector, THF eluent, vs. narrow PS standards), $Đ = M_w/M_n$.

temperatures;[64,65] it was possible to conduct epoxide ROP first at 60 °C and *ca.* 3 M initial AEC concentration. Full conversion was confirmed by ^{1}H NMR analysis of reaction aliquots, monitored by the disappearance of epoxide ring protons (*ca.* 4 h for 1 equiv. catalyst relative to P3HT-OH end-group). The solution was then cooled to room temperature (RT) and concentrated to drive ROP of the carbonate monomer, achieving typical conversions of 87–90% (Fig. S3). The ratio of PEO-EPO and AEC to P3HT-OH initiator was used to control the M_n of each block and overall triblock composition. Low P3HT contents (<10 wt%) were targeted, with the ionic block comprising 88–90 wt% of the final polymer. After acid-quenching of the base catalyst, the polymers were isolated by precipitation into cold pentane and washing with petroleum ether.

The ABC-triblock structure was verified by several methods. SEC analysis showed a clear increase in molar mass upon chain extension; for example, $M_{n,SEC}$ increased from 18.2 kg mol^{-1} ($Đ = 1.37$) for P3HT$_{110}$-OH to 109 kg mol^{-1} ($Đ = 2.02$) for isolated P3HT$_{110}$-*b*-P(EO-*g*-PEO)$_5$-*b*-PAEC$_{595}$ (PT110) (Fig. S4). End-group tests by ^{31}P{^{1}H} NMR spectroscopy confirmed successful macroinitiation through the disappearance of the P3HT-OH terminal signal at 148.99 ppm and the appearance of a new resonance at 148.27 ppm, consistent with the PAEC carbonate-OH chain end (Fig. S5). Block composition was determined by ^{1}H NMR analysis using the benzyl aromatic protons, with characteristic signals for PAEC (4.1 and 5.83 ppm) and P(EPO-*g*-PEG) (3.64 ppm). In addition to PT35 (DP$_{P3HT}$ = 35) and PT110 (DP$_{P3HT}$ = 110), a control polymer without P3HT (referred to as PT0) prepared by initiating ROP from benzyl alcohol, was synthesised for comparison. Full compositional data are summarised in Table 1.

To convert the pendant allyl groups of the polycarbonate block to alkali metal borates, an adapted two-step procedure was followed:[39] thiol–ene functionalisation to install diacid ligands, followed by coordination with boric acid and alkali metal carbonates (Fig. 1C). To ensure comparable polymer structures across the Li-, Na- and K-borate series, the diacid intermediate was prepared as a single batch and divided into three equal portions before metal coordination. Mercaptosuccinic acid (MSA) was selected as the thiol reagent due to its diacid functionality and potential for renewable sourcing. A two-fold excess of MSA was employed to ensure complete vinyl functionalisation while preventing crosslinking. The thiol–ene reaction was initiated photochemically using 2,2-dimethoxy-2-phenylacetophenone (DMPA). Reaction pro-

gress was monitored by ^{1}H NMR spectroscopy (DMSO-d$_6$), with complete vinyl conversion confirmed by disappearance of the allyl protons at 5.2–5.8 ppm and appearance of MSA-derived signals, including a broad carboxylic acid resonance at ~12 ppm. Subsequent metal borate formation was evidenced by loss of the carboxylic acid signal and appearance of a B–OH resonance at ~4.5 ppm (Fig. S7). The change in solubility from chloroform-soluble precursors to DMSO-soluble ionic products further supported successful functionalisation.

Multinuclear NMR spectroscopy confirmed the expected borate coordination environments: ^{11}B{^{1}H} NMR showed a dominant peak at 1.40 ppm, typical of mono-chelate tetrahedral sp^3 boron environments and consistent with previous findings that aliphatic polycarbonates preferentially form mono-chelate complexes.[39] As cation size increased, a growing signal at ~5.6 ppm suggested formation of some bis-tetrahedral chelates, likely stabilised by the larger ionic radius providing less sterically crowded coordination. ^{7}Li, ^{23}Na, and ^{39}K NMR confirmed single metal environments at −0.87, −0.03, and 9.13 ppm, respectively. Notably, sodium and potassium borate polymers with highest P3HT content (DP = 110) showed limited DMSO solubility, preventing complete NMR characterisation; however, successful functionalisation of the corresponding lithium analogues at this DP supported equivalent conversion across the series. The final polymers exhibited a characteristic colour progression ranging from pale pink (low P3HT content) through purple to nearly black (PT110), assumably reflecting increasing conjugation length and π–π stacking interactions.

Thermal and rheological properties

Polymer glass transition temperature (T_g) is often related to ionic conductivity *via* the Vogel–Tammann–Fulcher (VTF) equation, with lower T_g values being preferential for enhanced conductivity. DSC was used to assess the T_g of PT0, PT35 and PT110 Li-, Na- and K-borate CBEs. For the PT0 series (no P3HT block), T_g decreased when descending Group 1: −23, −26 and −39 °C for PT0Li, PT0Na and PT0K respectively (Fig. 2A). This trend is consistent with the variation in cation charge density. Li$^+$, having the smallest ionic radius (0.76 Å) and highest charge density, is expected to form the strongest interchain ionic crosslinks. Such crosslinks should restrict polymer backbone segmental motion, resulting in higher T_g. As ionic radius increases and charge density decreases, weaker ionic crosslinking permits greater chain flexibility, reflected in progressively lower T_g values for PT0Na and PT0K (Fig. 2B).
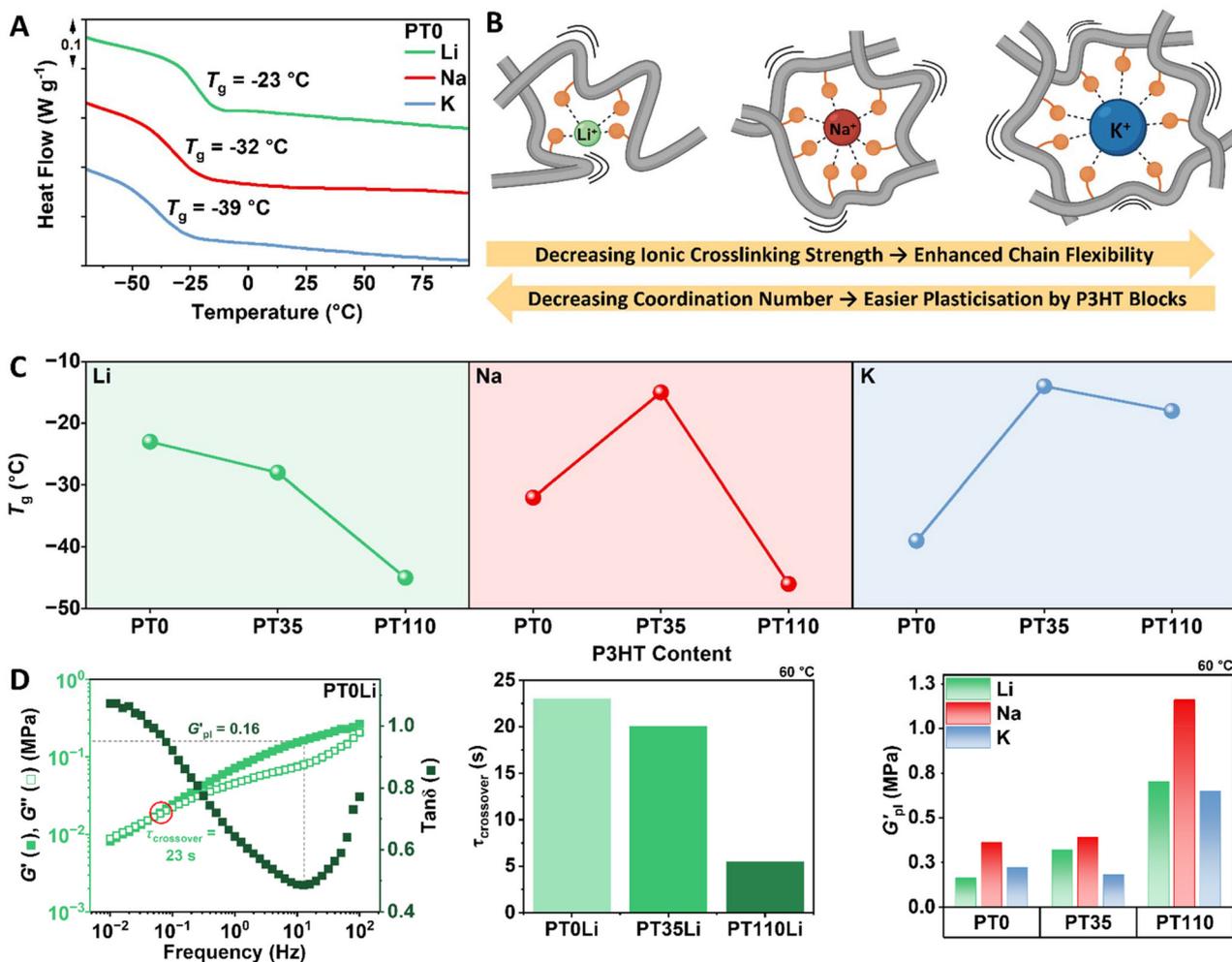
Fig. 2 (A) DSC traces for the PT0 series (Li⁺, Na⁺, K⁺). (B) Schematic illustrating how decreasing ionic crosslinking strength and increasing coordination number down the series are expected to influence T_g. (C) Measured T_g values as a function of P3HT DP for each cation (Li⁺ = green; Na⁺ = red; K⁺ = blue). (D) G'/G'' frequency sweeps for PT0Li (T = 60 °C) showing the crossover point, with corresponding relaxation timescales compared to PT35Li and PT110Li; determination of and comparison of G_{pl} values compared across series.

The effect of P3HT block length on T_g varied markedly with cation identity (Fig. 2C). For the lithium series, introduction of the short P3HT block (PT35Li) decreased T_g by 5 °C relative to PT0Li, with a further reduction to −45 °C for PT110Li. This behaviour is consistent with plasticisation of the lithium polyelectrolyte matrix by the P3HT block, with the effect increasing at higher P3HT DP. In contrast, the sodium series showed an initial increase in T_g for PT35Na before decreasing to −46 °C for PT110Na. For potassium, T_g increased for both PT35K and PT110K, by approximately 18 and 21 °C above PT0K respectively. We propose that whilst individual crosslink strength follows the order Li⁺ > Na⁺ > K⁺, the larger cations coordinate a greater number of polymer chains. As coordination number increases from 4 for Li⁺ to 6 for Na⁺ and 8 for K⁺, consistent with their crystallographic ionic radii, the resulting multichain crosslink junctions become more difficult for rigid P3HT blocks to disrupt. Consequently, for K⁺-based polyelectrolytes, the P3HT blocks are unable to effectively plasticise

the matrix, and T_g increases due to the additional chain stiffness introduced by the conjugated block. For Na⁺, only sufficiently long P3HT blocks can overcome the crosslinking and plasticise the matrix.

In support of this interpretation, parallel plate oscillatory rheology was conducted on the CBEs. Frequency sweeps were performed at strain amplitudes within the linear viscoelastic region at 10 °C temperature intervals from 30 to 70 °C. Only the Li⁺-polymers exhibited crossover of the elastic shear storage modulus (G') and viscous shear loss modulus (G'') at low frequencies and elevated temperatures, indicating liquid-like flow behaviour arising from the overcoming of ionic crosslinking interactions. Moreover, relaxation was faster (or occurred at lower temperatures) with increasing P3HT content: relaxation times of approximately 23, 20 and 6 seconds were observed for PT0Li, PT35Li and PT110Li respectively, supporting plasticisation and disruption of Li⁺ interchain crosslinking. Such low-frequency crossover points were not observed

for the Na- or K-series over the timescales and temperatures investigated, consistent with their stronger multi-chain cross-linking networks.

Notably, P3HT did impart a stiffening effect across all polymer series, as evidenced by the plateau modulus (G'_{pl}, corresponding to a minimum in $\tan\delta$). G'_{pl} increased with P3HT DP, and was higher for all DP110 samples. For Na$^+$ and K$^+$ at PT35, the impact on G'_{pl} was minimal (*ca.* 0.4 MPa for Na$^+$, 0.2 MPa for K$^+$), potentially indicating that the short P3HT block is insufficient to disrupt the ionic network at this composition. Na$^+$ polymers consistently exhibited the highest G'_{pl} values across the series at nearly 1.2 MPa at 60 °C for PT110Na.

The thermal stability of the conjugated polyelectrolytes, evaluated by thermogravimetric analysis (TGA, 10 °C min^{-1}, 30–500 °C, Fig. S10), placed constraints on the accessible temperature range for thermal and rheological characterisation. The onset of degradation ($T_{d,5\%}$) ranged from 105 to 168 °C across the series. Whilst this was lower than typical polycarbonates (>200 °C) and polyethers (>300 °C), it is likely sufficient for applications in biosensors and battery cells. For PT0, $T_{d,5\%}$ decreased slightly from Li$^+$ to K$^+$; PT0Li and PT35Li showed similar stability, while PT110 samples exhibited somewhat lower values. The multistep degradation profiles are characteristic of block copolymers with chemically distinct segments; residual coordinated DMSO may also contribute to early mass loss. This limited thermal window complicated assessment of phase separation in these block copolymers. Regioregular P3HT typically exhibits a clear T_m above 200 °C, which falls beyond the degradation onset for these materials while the glass transition is typically reported between 1 and 15 °C.[66,67] Nevertheless, each sample exhibited only a single T_g. This observation and particularly the decrease in T_g upon P3HT incorporation for the Li$^+$-series and PT110Na is inconsistent with classical microphase separation, which would yield two T_g values approaching those of the constituent homopolymers. The lack of phase-separated microstructure may instead point to polyelectrolyte complexation between the conjugated and ionic blocks, potentially facilitated by self-doping interactions.

Based on the VTF relationship, the measured T_g values would predict PT0K to exhibit the highest ionic conductivity among the PT0 series, owing to enhanced chain mobility. Among P3HT-containing polymers, the Li$^+$ series would be expected to improve with P3HT DP and PT110Na would be expected to exhibit the most favourable ionic conductivity. However, T_g reflects only segmental dynamics; ionic conductivity also depends on the extent of ion dissociation and intrinsic ion mobility, both of which vary with cation identity.

Ionic conductivity at low voltage

CBE samples were hot-pressed into films (*ca.* 0.9 mm thick) and analysed by electrochemical impedance spectroscopy (EIS) using gold blocking electrodes (6.35 mm diameter) under air-free, temperature-controlled conditions (see SI for details). The imaginary component of impedance was plotted against the

real component to give characteristic Nyquist plots, from which the bulk resistance (R_{bulk}) was determined by equivalent circuit fitting (Fig. 3A). Importantly, single semicircles and equivalent circuit fits indicated purely ionic conduction with no electronic contribution; mixed ionic-electronic conduction would manifest as two semicircles or require a circuit with more resistive elements. As discussed in the following section, electronic conductivity is only observed above a threshold applied voltage and is therefore absent under these low-voltage measurement conditions.

In contrast to the T_g trends for the PT0 series, Na$^+$ exhibited the highest ionic conductivity (σ_{ion}), reaching 10^{-4} S cm^{-1} over 30–70 °C, compared to 10^{-6} to 10^{-5} S cm^{-1} for Li$^+$ and 10^{-5} to 10^{-4} S cm^{-1} for K$^+$. Based on T_g alone, conductivity would be expected to follow K$^+$ > Na$^+$ > Li$^+$ owing to increasing chain mobility. Ion dissociation should also favour larger cations (K$^+$ > Na$^+$ > Li$^+$) due to weaker electrostatic interactions with the borate anion. However, intrinsic ion mobility follows the opposite trend (Li$^+$ > Na$^+$ > K$^+$) as smaller ions diffuse more readily through the polymer matrix. The observation that Na$^+$ exhibits the highest conductivity suggests it represents an optimal balance between ion dissociation and ion mobility.

Moreover, the response to incorporation of the P3HT blocks depended on cation identity (Fig. 3B and C). For the Li$^+$ series, ionic conductivity was essentially unaffected by the P3HT block despite its already noted impact on T_g and chain relaxation. For Na$^+$, which exhibited the highest conductivity overall, the short P3HT block (PT35Na) decreased ionic conductivity, whereas the longer block (PT110Na) provided improvements. For K$^+$, the short P3HT block improved conductivity, with longer blocks having limited additional impact.

To understand these contrasting behaviours, dielectric relaxation spectroscopy (DRS) was employed to probe polymer relaxation processes under an applied field, including segmental dynamics and ion–polymer coupling (Fig. 3D). For the Li$^+$ series, DRS revealed minimal differences between PT0Li, PT35Li and PT110Li, with similar timescales and intensities for both relaxation processes. VTF fits of the temperature-dependent conductivity, which account for T_g, showed a slight increase in activation energy (E_a) with P3HT content (Fig. 3B and S13–15). Together, these observations suggest that Li$^+$ transport is coordination-limited rather than segmental-limited, consistent with measurements conducted well above T_g for all polymers. We propose that disruption of the coordination network by P3HT (evidenced by faster bulk relaxation) results in less favourable hopping geometry, making it harder for tightly bound Li$^+$ to access and leave coordination sites.

For the Na$^+$ series, activation energy remained unchanged, suggesting that the observed conductivity differences arise primarily from changes in T_g or charge carrier concentration rather than a change in transport mechanism. The DRS response was more complex, with changes observed in both relaxation processes. Conductivity trends more closely followed T_g, which increased for PT35Na then decreased for PT110Na. Notably, PT110Na and PT110Li have similar T_g values (−45 to −46 °C), yet PT110Na exhibits higher conductivity, supporting

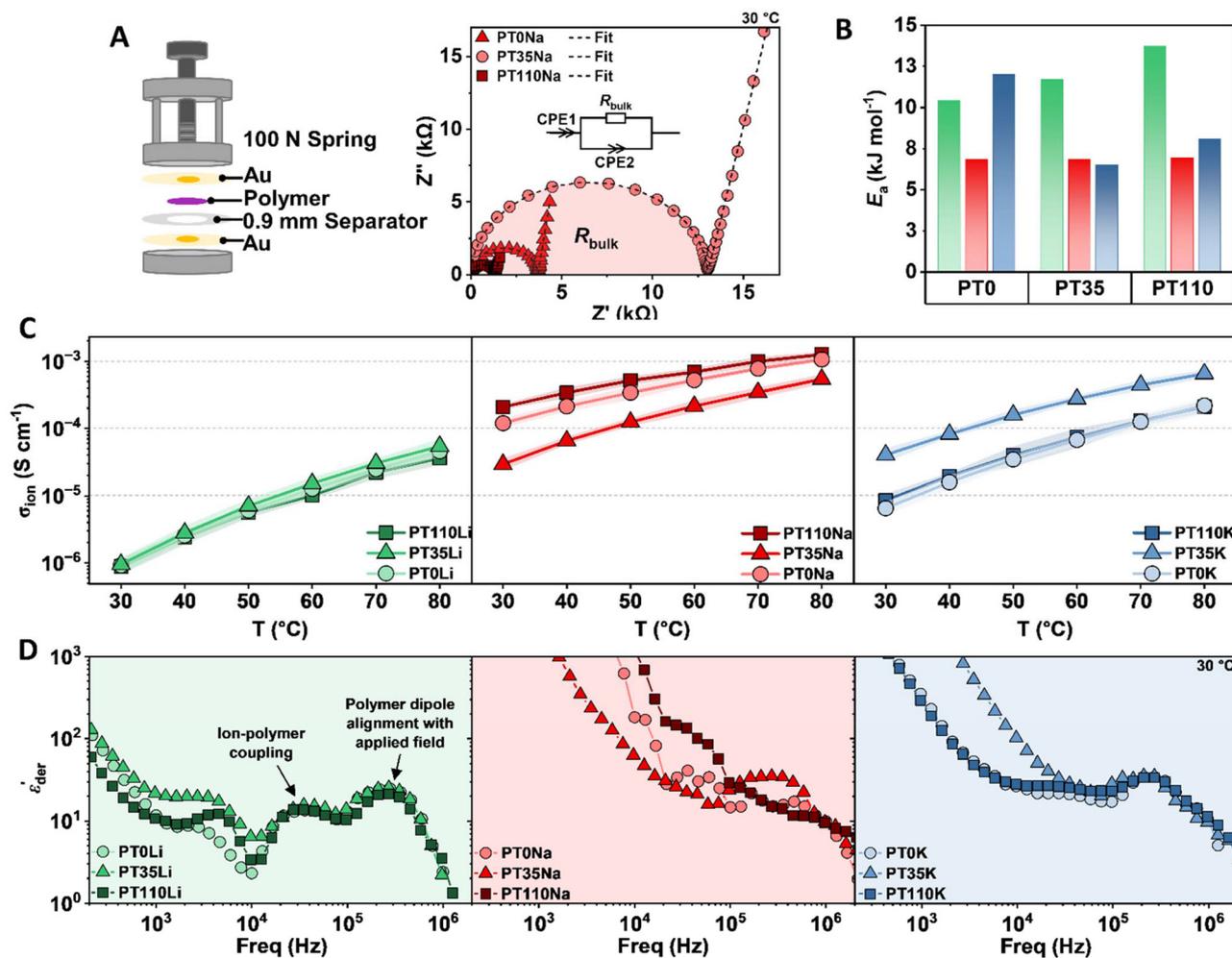
Fig. 3 Ionic transport. (A) Cell set-up for electrochemical impedance spectroscopy (EIS) with gold blocking electrodes, and representative Nyquist plots for Na⁺ series showing the equivalent circuit used to determine bulk resistance (data fit). (B) Activation energies calculated from VTF fits of the temperature-dependent ionic conductivity data shown in (C). (D) Dielectric relaxation spectra (DRS) probing frequency-dependent relaxations and ionic processes.

greater Na⁺ dissociation contributing to enhanced charge carrier concentration. PT110Na also showed the highest dielectric response in the ion–polymer coupling region compared to PT35Na and PT0Na, suggesting either more charge carriers or more efficient conduction pathways.

For the K⁺ series, PT35K exhibited the lowest activation energy. DRS showed a similar segmental relaxation peak (10⁵–10⁶ Hz) across the series, but the ion–polymer coupling peak (10⁴–10⁵ Hz) was less clearly defined compared to Li⁺ and Na⁺, and was most pronounced for PT35K. This suggests that moderate P3HT content optimises the local coordination environment for K⁺ hopping, reducing the energy barrier for transport. The larger K⁺ ion, with its higher coordination number and weaker individual crosslinks, may benefit from structural reorganisation introduced by short P3HT blocks without the excessive rigidity imparted by longer conjugated segments. Medium M_n CPE-K has been shown elsewhere to provide enhanced charge transport pathways and electrical properties

attributed to molecular packing and orientation of packing orders.[31]

Voltage-activated electronic conductivity

An applied voltage is required to activate the electronic conductivity in these systems. Linear sweep voltammetry (LSV) was performed by applying a positive voltage ramp to the films at 1 mV s⁻¹. The resulting current–voltage (I–V) curves revealed a rapid increase in current at certain threshold voltages for all P3HT-containing samples (Fig. 4A). Threshold voltages for these inflection points were dependent on P3HT block length and cation identity but were typically observed around 1–1.5 V. No inflection was observed for PT0 samples, confirming that the electronic response originates from the P3HT block. This voltage-gating behaviour is consistent with percolation theory for conjugated polymers, where electronic transport is initially limited by isolated conjugated domains. Above the threshold, electronic conduction is enabled through field-induced align-
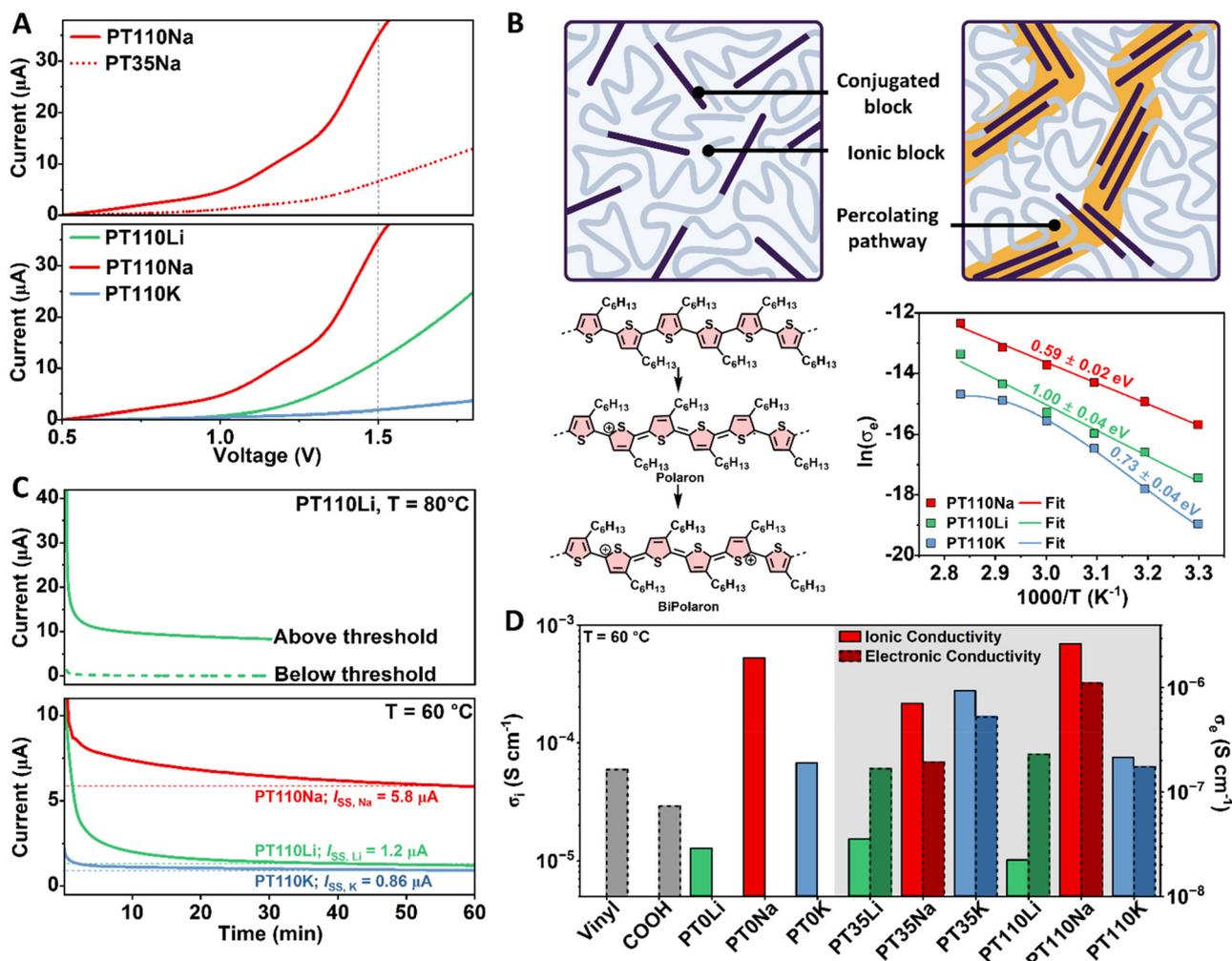
Fig. 4 Electronic conductivity. (A) Linear sweep voltammetry (1 mV s^{-1} scan rate) showing threshold voltages; dashed line indicates 1.5 V applied for chronoamperometry. (B) Schematic of proposed (bi)polarons and alignment mechanism, with temperature dependence of electronic conductivity and determined activation energies (eV). (C) Chronoamperometry measurements showing steady-state current (I_{ss}) used to determine electronic conductivity. (D) Summary of mixed conductivity at 60 °C including controls: vinyl-, COOH-functionalised triblock copolymers (pre-borate) and PT0 (no P3HT).

ment and oxidation of P3HT to generate positive polarons that hop along the conjugated backbone and between chains. Polarons may already be present from ground-state doping by the proximal borate anions. In either case, the borate provides charge compensation for the oxidised conjugated segments, effectively creating a self-doped system. Due to the low weight fraction of P3HT in these systems, an applied voltage is required to establish percolating networks through which polarons can traverse the film. In general, PT110 samples exhibited lower threshold voltages than PT35, likely due to improved connectivity between longer conjugated domains facilitating percolation. The threshold voltage also depended on cation identity, following Na$^+$ < Li$^+$ < K$^+$ for the PT110 series. This trend mirrors that of ionic conductivity suggesting that borate mobility influences polaron stabilisation.

To quantify electronic conductivity (σ_e) separately from ionic contributions, chronoamperometry (CA) was performed (Fig. 4B).

A constant voltage of 1.5 V (above the threshold for all samples) was applied, and the resulting current was monitored as a function of time until steady state was reached (at least 1 h at 60 °C). At early times, the current reflects both ionic and electronic contributions; at long times, ion motion ceases at the blocking gold electrodes, and the plateau current is purely electronic. For PT0 samples, current decayed to negligible values, confirming the absence of electronic pathways. Similarly, when voltages below the threshold (0.1 V) were applied to P3HT-containing samples, current decayed to zero, confirming that the residual steady-state current at 1.5 V arises from electronic conduction. Steady-state currents were highest for PT110Na, followed by PT110Li and PT110K. Electronic conductivity was calculated from the steady-state current using sample thickness (0.9 mm), applied voltage (1.5 V), and electrode cross-sectional area (31.67 mm^2).

The temperature dependence of electronic conductivity was used to extract activation energies (E_a). PT110Na exhibited the

lowest E_a, followed by PT110Li and PT110K, with PT110Na also showing the highest absolute conductivity values (Fig. 4C). The non-linearity observed for PT110K at higher temperatures may indicate the onset of phase separation or change in morphology. Values for PT35 samples were less stable and showed poorer linearity, possibly reflecting less well-defined percolating networks at shorter P3HT block lengths (Fig. S16). Control experiments on vinyl- and diacid-functionalised precursors (prior to borate conversion) also exhibited electronic conductivity, with the vinyl precursor outperforming the diacid (Fig. S17). Notably, PT110Na and PT35K exceeded both controls, while other borate samples showed comparable values (Fig. 4D). The poor performance of the diacid precursor may arise from interchain hydrogen bonding that restricts backbone mobility and hinders polaron delocalisation. Conversion to the borate removes this constraint and provides electrostatic stabilisation of positive polarons, but realising enhanced electronic transport requires the appropriate combination of cation identity and P3HT block length.

At 60 °C, PT110Na exhibited both the highest ionic conductivity ($\sigma_i = 10^{-4}$ S cm^{-1}) and electronic conductivity ($\sigma_e = 10^{-6}$ S cm^{-1}), demonstrating mixed ionic-electronic character. These results highlight the dual role of the borate anion: it enables cation transport through dissociation (ionic conductivity) and polaron stabilisation through charge compensation (electronic conductivity). Cation identity controls how readily the borate dissociates, which in turn affects both conduction mechanisms. This tunability offers a route to tailoring mixed conductors for specific applications through appropriate cation selection.

Given the promising performance of PT110Na, we synthesised sodium borate CBEs with increased P3HT content: PT160Na (20 wt% P3HT) and PT220Na (50 wt% P3HT). Electronic conductivity increased relative to PT110Na for both samples, reaching 10^{-5} S cm^{-1} for PT220Na (Fig. 5 and S18). For PT220Na, ionic conductivity also improved to 10^{-3} S cm^{-1} at 60 °C, representing an example of simultaneous enhancement of both ionic and electronic transport. With comparable thickness films, the onset voltage for 50 wt% occurred noticeable earlier around 0.6 V compared to >1 V for PT110Na. Direct comparison to literature values is complicated by differences in measurement conditions, film thickness, and polymer architecture; nevertheless, these conductivities position these borate CBEs as promising candidates for applications requiring balanced mixed conduction.

Cation coordination environments: DFT calculations

DFT calculations were performed to provide molecular-level insight into the cation–borate interactions. To reduce computational time, model triblock structures comprising one P3HT unit, one EPO-PEG unit (PEG = 4 EO repeat units), and one carbonate-borate unit were initially used; extending to three thiophene repeat units gave similar binding energies (Table S2), confirming the smaller model adequately captures these interactions. Geometry optimisations yielded favourable binding energies (ΔG) for Li$^+$, Na$^+$, and K$^+$ at the borate site alone, averaging -4.29 ± 0.63 kcal mol^{-1} (Fig. 6A). The similar values across cations likely reflect the single-chain model, which does not capture multi-chain coordination environments. However, alkali metal cations may also achieve coordination sphere satisfaction through the PEO ether oxygens rather than, or in addition to, the borate anion. When cations were coordinated solely by PEO oxygens and fully dissociated from the borate, the average binding energy was -16.5 ± 0.8 kcal mol^{-1}. With the borate anion still involved in the coordination sphere, Li$^+$ and Na$^+$ showed more favourable binding energies of -19.9 and -19.2 kcal mol^{-1} respectively, whereas K$^+$ was less favourable at -14.7 kcal mol^{-1}. The latter was close to its fully dissociated ether-coordinated value of -15.9 kcal mol^{-1}. Coordination environments involving the thiophene sulfur were less favourable at -14.1 ± 0.9 kcal mol^{-1}.

These results support the role of the PEO side chain in promoting cation dissociation from the borate, consistent with our previous findings demonstrating improved ionic conductivities with neighbouring PEO block segments to polycarbonate lithium borates.[39] The strongly favourable binding energies for Li$^+$ with borate involvement support the interpretation of coordination-limited ionic conductivity arising from tightly held Li$^+$ ions. In contrast, K$^+$ showed a smaller spread in binding energies across borate-involved, PEO-only, and thiophene-coordinated environments ($\Delta 2.7$ kcal mol^{-1}, *cf. ca.* 5.0 kcal mol^{-1} for Li$^+$ and Na$^+$), suggesting weaker preference between coordination sites. This is consistent with the generally flatter DRS spectra observed for K$^+$ compared to Li$^+$ and Na$^+$. However, PT35K showed a notably higher dielectric response than PT0K or PT110K. The similar binding energies suggest K$^+$ may be uniquely able to interact with the thiophene sulfur, an environment that is less energetically accessible to Li$^+$ and Na$^+$ and at moderate P3HT content, this additional coordination pathway may enhance ion–polymer coupling.

Finally, we considered the impact of polaron and bipolaron formation on cation–polymer interactions (Fig. 6B). A polaron is generated by one-electron oxidation of the P3HT backbone, yielding a positive charge and unpaired electron; removal of a second electron produces a spinless, doubly-charged bipo-
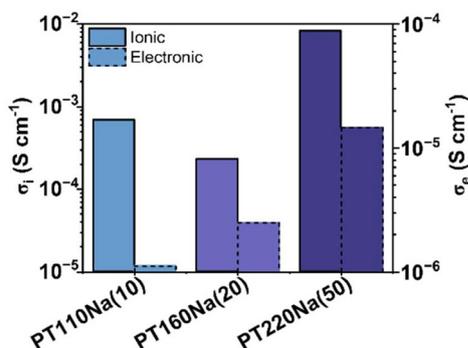

Fig. 5 Ionic and electronic conductivity at 60 °C for Na-CBEs with varying P3HT wt%: 10 (PT110Na above), 20 wt% P3HT, DP$_{P3HT}$ = 160 and 50 wt% P3HT, DP$_{P3HT}$ = 220.
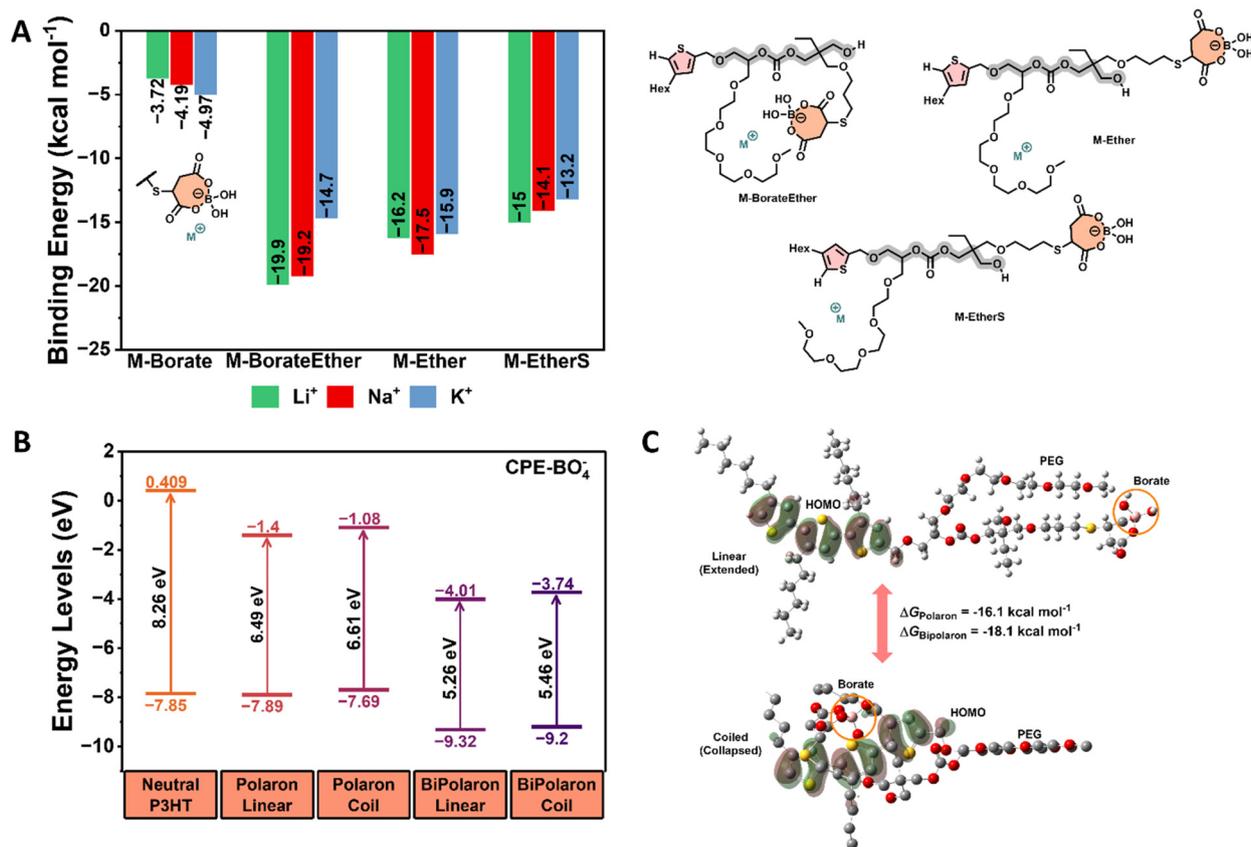
Fig. 6 DFT computations (ωB97XD/6-311G(d,p)/cpcm, solvent = DMSO). (A) Cation binding energies in different coordination environments. (B) HOMO–LUMO energies for neutral, polaron, and bipolaron states. Note, for bipolaron systems, the formal HOMO is localised on the borate and hence, the P3HT backbone-localised HOMO−1 is shown for comparison. (C) Relative $\Delta\Delta G$ for coiled and linear conformations with HOMO surfaces for the polaron shown.

laron. In anionic conjugated polyelectrolytes, polarons can form without external doping through self-doping by the tethered anion, introducing electrostatic interactions between the resulting positive charge on the backbone and the borate. DFT calculations were used to compare extended (linear) and collapsed (coiled) conformations in which the borate is positioned close to the oxidised backbone. For the anionic CBE without a metal cation, the coiled conformation is thermodynamically favoured by 16.1 kcal mol^{-1} for the polaron and 18.1 kcal mol^{-1} for the bipolaron, consistent with electrostatic stabilisation between the anionic borate and the cationic backbone (Fig. 6C). This conformational preference seems to occur with minimal perturbation to the electronic structure: HOMO–LUMO gaps differ by only 0.12 eV between linear and coiled polaron conformers (6.49 vs. 6.61 eV) and 0.20 eV for the bipolaron (5.26 vs. 5.46 eV). The HOMO–LUMO gap closes progressively, as expected from neutral to polaron to bipolaron as oxidation introduces mid-gap states, and the HOMO is stabilised as expected upon oxidation (Table S3).[68] For linear conformations containing Li$^+$, Na$^+$, and K$^+$, frontier orbital energies are comparable to the linear metal-free anionic system, indicating that cation identity has minimal direct impact on the electronic structure of the oxidised backbone (Table S3).

Mechanical properties

Mechanical compliance is important for conjugated polyelectrolyte applications, particularly at bioelectronic interfaces where matching tissue moduli is desirable.[69] Semiconducting and ionic polymers in devices require durability, and tensile response can be an important predictor of performance. Lipomi and coworkers have demonstrated the advantages block copolymers can offer over blended systems in terms of mechanical stretchability and toughness.[70,71] The mechanical properties of the CBEs were assessed by uniaxial tensile testing. Dumbbell specimens (ISO 527-type 5B) were subjected to tensile testing at strain rates of 10, 50 and 100 mm min^{-1} to obtain stress–strain curves, from which Young's moduli (E_y) were determined at low strain (Fig. 7A).

PT35Li exhibited a higher Young's modulus than PT35Na (80 kPa vs. 6 kPa), consistent with stronger ionic crosslinking for Li$^+$ compared to Na$^+$. These values are comparable to those reported for biological tissues: PT35Na falls within the range for cardiac muscle (5–50 kPa), while PT35Li is comparable to skin (60 kPa–1 MPa) (Fig. S20). At 10 mm min^{-1}, PT35Li and PT35Na exhibited elongation at break of 324% and 183% respectively, with tensile strengths of 290 and 32 kPa. PT35K
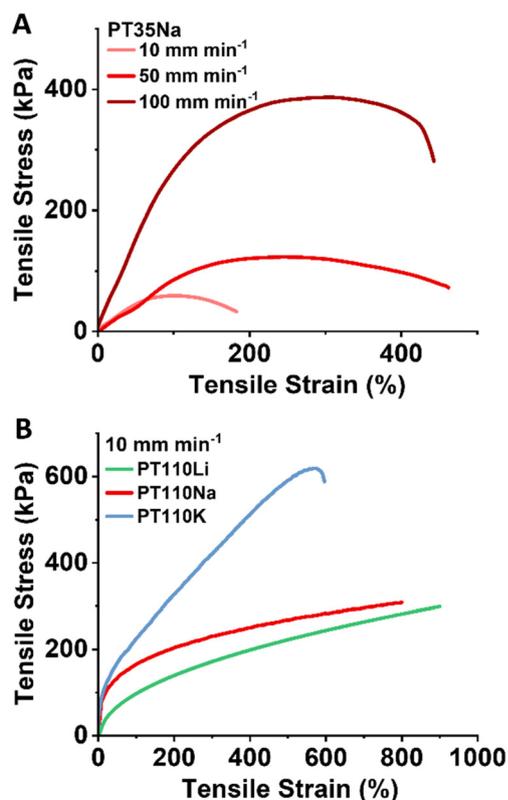
Fig. 7 Mechanical performances of CBE films: (A) stress–strain curves for PT35Na at varying strain rates. (B) Stress–strain curves for the PT110 series at fixed strain rate.

was too mechanically weak to test reliably, consistent with its weaker ionic crosslinking network.

For PT110, all three cation variants could be compared. Tensile strength followed $K^+ > Na^+ > Li^+$ (Fig. 7B). This contrasts with PT35, where PT35K was too weak to test. The reversal may reflect the different roles of K^+ at low *versus* high P3HT content echoed in the ionic conductivity. At low P3HT content, weak ionic crosslinking dominates and K^+ provides insufficient mechanical reinforcement; at higher P3HT content, K^+ interactions with the thiophene backbone as suggested by the DFT calculations may contribute to a more robust network. Generally, PT110 samples showed higher tensile strength and elongation at break than PT35, reflecting the rigidifying effect of P3HT (increased G'_{pl}). For example, PT110Na exhibited elongation at break of nearly 800% *versus* <200% for PT35Na at the same strain rate, and tensile strengths of >200 kPa *versus* <100 kPa.

Conclusions

Conjugated polyelectrolytes with a block copolymer architecture, comprising P3HT linked to anionic borate-functionalised polycarbonates with PEO side chains, were synthesised *via* SCTP and organocatalysed ROP with Li⁺, Na⁺ and K⁺ counterca-

tions. This block design contrasts with the blends or pendant ionic systems typically reported for mixed ionic-electronic conductors. At low voltage, conduction was purely ionic, with Na⁺ exhibiting the highest conductivity (10^{-4} S cm⁻¹), attributed to an optimal balance between ion dissociation and mobility; DFT calculations supported the role of PEO ether oxygens in facilitating cation dissociation from the borate. Above a threshold voltage, electronic conduction was activated through polaron formation on the P3HT backbone, with the borate anion providing charge compensation. Na⁺ polymers exhibited both the highest ionic and electronic conductivity, demonstrating that the borate anion serves a dual role: enabling cation transport and stabilising polarons. The response to P3HT block length was cation-dependent, providing a design parameter orthogonal to cation selection. Increasing P3HT content to 50 wt% further enhanced both ionic (10^{-3} S cm⁻¹) and electronic (10^{-5} S cm⁻¹) conductivity. With Young's moduli of 6–80 kPa and voltage-switchable transport, these conjugated polyelectrolytes offer a tuneable materials platform for applications demanding both ionic and electronic function at soft tissue interfaces.

Author contributions

S. L.: data curation, methodology, investigation, validation, writing – reviewing and editing. S. F.: data curation, methodology, investigation, validation, writing – reviewing and editing. G. L. G.: writing – original draft, reviewing and editing, visualization, supervision, project administration, funding acquisition and conceptualization.

Conflicts of interest

There are no conflicts to declare.

Data availability

The data supporting this article has been included as part of the supplementary information (SI). Supplementary information: full experimental details including materials and methods, characterisation techniques, monomer and polymer ^{1}H, ^{13}C, ^{11}B NMR spectra; MALDI-ToF mass spectrometry, SEC traces; DSC thermograms; EIS Nyquist plots, VTF fits, *I–V* curves; computational details and DFT energies (Hartree). See DOI: https://doi.org/10.1039/d6py00119j.

Optimised DFT structures are available at: https://github.com/GeorgeLGregory/Conjugated-Polyelectrolytes-CPEs-DFT-Structures.

Acknowledgements

We thank the Royal Society Dorothy Hodgkin Fellowship (DHF \R1\221101) and Royal Society enhanced research expenses

References

1 N. Cao, Y. Lang, G. Gu, X. Jia and D. Chao, *Adv. Funct. Mater.*, 2025, e17668.

2 G. Quek, B. Roehrich, Y. Su, L. Sepunaru and G. C. Bazan, *Adv. Mater.*, 2022, **34**, 2104206.

3 H. Kim, Y. Won, H. W. Song, Y. Kwon, M. Jun and J. H. Oh, *Adv. Sci.*, 2024, **11**, 2306191.

4 J. Song, L. Li, W.-Y. Wong and F. Yan, *Acc. Mater. Res.*, 2024, **5**, 1036–1047.

5 J. H. Park, Y. W. Noh, J. M. Ha, A. K. Harit, A. Tripathi, J. Lee, B. R. Lee, M. H. Song and H. Y. Woo, *ACS Appl. Mater. Interfaces*, 2024, **16**, 19937–19946.

6 T. Nguyen-Dang, S. Chae, J. Chatsirisupachai, H. Wakidi, V. Promarak, Y. Visell and T.-Q. Nguyen, *Adv. Mater.*, 2022, **34**, 2200274.

7 G. Pace, A. Zele, P. Nguyen, R. J. Clément and R. A. Segalman, *Chem. Mater.*, 2023, **35**, 8101–8111.

8 H. An, X. Li, K. A. Smith, Y. Zhang, R. Verduzco and J. L. Lutkenhaus, *ACS Appl. Energy Mater.*, 2018, **1**, 5919–5927.

9 P. Das, R. Elizalde-Segovia, B. Zayat, C. Z. Salamat, G. Pace, K. Zhai, R. C. Vincent, B. S. Dunn, R. A. Segalman, S. H. Tolbert, S. R. Narayan and B. C. Thompson, *Chem. Mater.*, 2022, **34**, 2672–2686.

10 J. Tropp, D. Meli and J. Rivnay, *Matter*, 2023, **6**, 3132–3164.

11 Y. Wang, S. Wustoni, J. Surgailis, Y. Zhong and A. Koklu, *Nat. Rev. Mater.*, 2024, **9**, 249–265.

12 W. He, Y. Kashino, N. Nozaki, J. Kimpel, H. Matsumoto, Y. Hayamizu and T. Michinobu, *J. Mater. Chem. C*, 2024, **12**, 18282–18290.

13 P. Ghosh and P. K. Iyer, *ACS Appl. Mater. Interfaces*, 2024, **16**, 20034–20054.

14 A. T. Lill, D. X. Cao, M. Schrock, J. Vollbrecht, J. Huang, T. Nguyen-Dang, V. V. Brus, B. Yurash, D. Leifert, G. C. Bazan and T.-Q. Nguyen, *Adv. Mater.*, 2020, **32**, 1908120.

15 W. Lee, J. L. Chouhan, A. K. Harit, C. Park, D. Kim, S. R. McCuskey, G. C. Bazan and H. Y. Woo, *ACS Nano*, 2025, **19**, 5938–5965.

16 P. Das, A. Zele, M.-P. Lin, J. T. Mefford, M. L. Chabinyc and R. A. Segalman, *ACS Macro Lett.*, 2025, **14**, 925–932.

17 C. L. Anderson, N. Dai, S. J. Teat, B. He, S. Wang and Y. Liu, *Angew. Chem., Int. Ed.*, 2019, **58**, 17978–17985.

18 P. A. Finn, I. E. Jacobs, J. Armitage, R. Wu, B. D. Paulsen, M. Freeley, M. Palma, J. Rivnay, H. Sirringhaus and C. B. Nielsen, *J. Mater. Chem. C*, 2020, **8**, 16216–16223.

19 G. Pace, O. Nordness, K. Asham, R. J. Clément and R. A. Segalman, *Chem. Mater.*, 2022, **34**, 4672–4681.

20 P. Schmode, A. Savva, R. Kahl, D. Ohayon, F. Meichsner, O. Dolynchuk, T. Thurn-Albrecht, S. Inal and M. Thelakkat, *ACS Appl. Mater. Interfaces*, 2020, **12**, 13029–13039.

21 G. Pace, O. Nordness, P. H. Nguyen, Y.-J. Choi, C. Tran, R. J. Clément and R. A. Segalman, *Macromolecules*, 2023, **56**, 6078–6085.

22 H. Yan, S. Cong, M. Daboczi, S. Limbu, I. Hamilton, S. Kwon, C. L. Rapley, S. M. Tahir, G. Kerherve, D. Payne, M. Heeney and J.-S. Kim, *Adv. Opt. Mater.*, 2023, **11**, 2300988.

23 S. P. O. Danielsen, B. J. Thompson, G. H. Fredrickson, T.-Q. Nguyen, G. C. Bazan and R. A. Segalman, *Macromolecules*, 2022, **55**, 3437–3448.

24 C. Zhang, L. Yao, M. Pu and C. Zhou, *RSC Appl. Polym.*, 2025, **3**, 549–573.

25 B. D. Paulsen, K. Tybrandt, E. Stavrinidou and J. Rivnay, *Nat. Mater.*, 2020, **19**, 13–26.

26 H. Sun, I. Barboza-Ramos, X. Wang and K. S. Schanze, *ACS Appl. Mater. Interfaces*, 2024, **16**, 20023–20033.

27 S. Fabiano, L. Flagg, T. C. Hidalgo Castillo, S. Inal, L. G. Kaake, L. V. Kayser, S. T. Keene, S. Ludwigs, C. Muller, B. M. Savoie, B. Lüssem, J. L. Lutkenhaus, M. Matta, D. Meli, S. N. Patel, B. D. Paulsen, J. Rivnay and J. Surgailis, *J. Mater. Chem. C*, 2023, **11**, 14527–14539.

28 E. M. Thomas, P. H. Nguyen, S. D. Jones, M. L. Chabinyc and R. A. Segalman, *Annu. Rev. Mater. Res.*, 2021, **51**, 1–20.

29 K. Stewart, K. Pagano, E. Tan, M. Daboczi, M. Rimmele, J. Luke, S. Eslava and J.-S. Kim, *Adv. Mater.*, 2024, **36**, 2211184.

30 C. K. Mai, H. Zhou, Y. Zhang, Z. B. Henson, T. Q. Nguyen, A. J. Heeger and G. C. Bazan, *Angew. Chem., Int. Ed.*, 2013, **52**, 12874–12878.

31 S. Chae, T. Nguyen-Dang, J. Chatsirisupachai, A. Yi, R. J. Vázquez, G. Quek, V. Promarak, H. J. Kim, G. C. Bazan and T.-Q. Nguyen, *Adv. Funct. Mater.*, 2024, **34**, 2310852.

32 C.-K. Mai, R. A. Schlitz, G. M. Su, D. Spitzer, X. Wang, S. L. Fronk, D. G. Cahill, M. L. Chabinyc and G. C. Bazan, *J. Am. Chem. Soc.*, 2014, **136**, 13478–13481.

33 B. D. Paulsen, S. Fabiano and J. Rivnay, *Annu. Rev. Mater. Res.*, 2021, **51**, 73–99.

34 H. Singh, I. Popov, M. L. Lehmann, M. A. Rahman, K. S. Schweizer, R. Kumar, T. Saito, A. P. Sokolov and C. P. Gainaru, *ACS Appl. Polym. Mater.*, 2025, **7**, 9661–9668.

35 N. D. Kirchhofer, S. R. McCuskey, C.-K. Mai and G. C. Bazan, *Angew. Chem., Int. Ed.*, 2017, **56**, 6519–6522.

36 J. Wagner, Y. Song, T. Lee and H. E. Katz, *Electrochem. Sci. Adv.*, 2022, **2**, e2100165.

37 D.-M. Shin, J. E. Bachman, M. K. Taylor, J. Kamcev, J. G. Park, M. E. Ziebel, E. Velasquez, N. N. Jarenwattananon, G. K. Sethi, Y. Cui and J. R. Long, *Adv. Mater.*, 2020, **32**, 1905771.

38 G. Guzmán-González, S. Vauthier, M. Alvarez-Tirado, S. Cotte, L. Castro, A. Guéguen, N. Casado and D. Mecerreyes, *Angew. Chem., Int. Ed.*, 2022, **61**, e202114024.

39 T. Charlesworth, K. Yiamsawat, H. Gao, G. J. Rees, C. K. Williams, P. G. Bruce, M. Pasta and G. L. Gregory, *Angew. Chem., Int. Ed.*, 2024, **63**, e202408246.

40 F. J. Leslie, K. G. Stakem and G. L. Gregory, *ChemSusChem*, 2025, **18**, e202500055.

41 K. N. Baustert, J. H. Bombile, M. T. Rahman, A. O. Yusuf, R. Li, A. J. Huckaba, C. Risko and K. R. Graham, *Adv. Mater.*, 2024, **36**, 2313863.

42 D. M. Friday and N. E. Jackson, *Macromolecules*, 2022, **55**, 1866–1877.

43 Z. Zujovic, E. W. C. Chan and J. Travas-Sejdic, *Macromolecules*, 2024, **57**, 7123–7137.

44 P. Cavassin, T. C. Hidalgo Castillo, R. Marcial-Hernandez, P. Gilhooly-Finn, J. Réhault, S. Inal, C. B. Nielsen and N. Banerji, *Chem. Mater.*, 2025, **37**, 6983–6990.

45 A. A. Advincula, A. Atassi, S. A. Gregory, K. J. Thorley, J. F. Ponder Jr., G. Freychet, A. L. Jones, G. M. Su, S. K. Yee and J. R. Reynolds, *ACS Appl. Mater. Interfaces*, 2023, **15**, 35227–35238.

46 B. X. Dong, C. Nowak, J. W. Onorato, J. Strzalka, F. A. Escobedo, C. K. Luscombe, P. F. Nealey and S. N. Patel, *Chem. Mater.*, 2019, **31**, 1418–1429.

47 S. N. Patel, A. E. Javier and N. P. Balsara, *ACS Nano*, 2013, **7**, 6056–6068.

48 S. N. Patel, A. E. Javier, G. M. Stone, S. A. Mullin and N. P. Balsara, *ACS Nano*, 2012, **6**, 1589–1600.

49 B. X. Dong, Z. Liu, J. W. Onorato, T. Ma, J. Strzalka, P. Bennington, C. K. Luscombe, C. K. Ober, P. F. Nealey and S. N. Patel, *Adv. Funct. Mater.*, 2021, **31**, 2106991.

50 C.-Y. Li, G.-H. Jiang, T. Higashihara and Y.-C. Lin, *ACS Appl. Mater. Interfaces*, 2024, **16**, 52753–52765.

51 P. M. Reichstein, J. C. Brendel, M. Drechsler and M. Thelakkat, *ACS Appl. Nano Mater.*, 2019, **2**, 2133–2143.

52 H. Erothu, J. Kolomanska, P. Johnston, S. Schumann, D. Deribew, D. T. W. Toolan, A. Gregori, C. Dagron-Lartigau, G. Portale, W. Bras, T. Arnold, A. Distler, R. C. Hiorns, P. Mokarian-Tabari, T. W. Collins, J. R. Howse and P. D. Topham, *Macromolecules*, 2015, **48**, 2107–2117.

53 S. Yao, A. Bethani, N. Ziane, C. Brochon, G. Fleury, G. Hadziioannou, P. Poulin, J.-B. Salmon and E. Cloutet, *Macromolecules*, 2015, **48**, 7473–7480.

54 J. Wang, C. Guo, Y. Yu, H. Yin, X. Liu and Y. Jiang, *RSC Adv.*, 2015, **5**, 17905–17914.

55 J. Lee, H. Park, S.-H. Hwang, I.-H. Lee and T.-L. Choi, *Macromolecules*, 2020, **53**, 3306–3314.

56 K.-B. Seo, I.-H. Lee, J. Lee, I. Choi and T.-L. Choi, *J. Am. Chem. Soc.*, 2018, **140**, 4335–4343.

57 H. Park, J. Lee, S.-H. Hwang, D. Kim, S. H. Hong and T.-L. Choi, *Macromolecules*, 2022, **55**, 3476–3483.

58 J. Lee, H. Kim, H. Park, T. Kim, S.-H. Hwang, D. Seo, T. D. Chung and T.-L. Choi, *J. Am. Chem. Soc.*, 2021, **143**, 11180–11190.

59 H.-N. Choi, H.-S. Yang, J.-H. Chae, T.-L. Choi and I.-H. Lee, *Macromolecules*, 2020, **53**, 5497–5503.

60 H.-N. Choi, H.-S. Yang, S. Park, T.-L. Choi and I.-H. Lee, *Macromolecules*, 2024, **57**, 8050–8058.

61 H.-N. Choi and I.-H. Lee, *Polym. J.*, 2021, **53**, 1205–1211.

62 J. A. Carrillo, M. J. Ingleson and M. L. Turner, *Macromolecules*, 2015, **48**, 979–986.

63 J. Mindemark, L. Imholt, J. Montero and D. Brandell, *J. Polym. Sci., Part A: Polym. Chem.*, 2016, **54**, 2128–2135.

64 R. M. R. Reese, A. M. Ganose and C. Romain, *Faraday Discuss.*, 2026, **262**, 455–477.

65 V. Nieboer, J. Wohlert, P. Olsén and K. Odelius, *Faraday Discuss.*, 2026, **262**, 311–326.

66 S. Savagatrup, A. D. Printz, H. Wu, K. M. Rajan, E. J. Sawyer, A. V. Zaretski, C. J. Bettinger and D. J. Lipomi, *Synth. Met.*, 2015, **203**, 208–214.

67 R. Xie, A. R. Weisen, Y. Lee, M. A. Aplan, A. M. Fenton, A. E. Masucci, F. Kempe, M. Sommer, C. W. Pester, R. H. Colby and E. D. Gomez, *Nat. Commun.*, 2020, **11**, 893.

68 E. C. Wu and B. J. Schwartz, *J. Chem. Theory Comput.*, 2023, **19**, 6761–6769.

69 R. Blau, A. X. Chen, B. Polat, L. L. Becerra, R. Runser, B. Zamanimeymian, K. Choudhary and D. J. Lipomi, *ACS Appl. Mater. Interfaces*, 2022, **14**, 4823–4835.

70 L. V. Kayser, M. D. Russell, D. Rodriquez, S. N. Abuhamdieh, C. Dhong, S. Khan, A. N. Stein, J. Ramírez and D. J. Lipomi, *Chem. Mater.*, 2018, **30**, 4459–4468.

71 R. Blau, A. Abdal, N. Root, A. X. Chen, T. Rafeedi, R. Ramji, Y. Qie, T. Kim, A. Navarro, J. Chin, L. L. Becerra, S. J. Edmunds, S. M. Russman, S. A. Dayeh, D. P. Fenning, R. Rouw and D. J. Lipomi, *Sci. Rob.*, 2024, **9**, eadk3925.